Anchored Cu(II) tetra(4-carboxylphenyl)porphyrin to P25 (TiO2) for efficient photocatalytic ability in CO2 reduction

Lei Wang[a], Shuhua Duan[a], Pengxia Jin[a], Houde She[a], Jingwei Huang[a], Ziqiang Lei[a], Tierui Zhang[b], Qizhao Wang[a],*

[a] College of Chemistry and Chemical Engineering, Key Laboratory of Eco-Environment-Related Polymer Materials, Ministry of Education of China, Northwest Normal University, Lanzhou, 730070, China
[b] Key Laboratory of Photochemical Conversion and Optoelectronic Materials, Technical Institute of Physics and Chemistry, Chinese Academy of Sciences, Beijing, 100190, China

ARTICLE INFO

ABSTRACT

The exploration of photocatalysts used in converting CO_2 into applicable organic products is of significant importance for addressing the universal problems of both global warming and energy shortage. In this work, the sensitizer Cu(II) tetra(4-carboxylphenyl)porphyrin (CuTCPP) was successfully combined with hydroxylated commercial P25 (TiO_2) by hydrothermal treatment (denoted as $P25_m$). The as-prepared composite CuTCPP/$P25_m$ shows photocatalytic activity for CO_2 reduction to give methane under UV-vis irradiation. The characterizations entailed in our work not only confirm the effective combination of the composite, but exhibit a stronger light absorption capability than $P25_m$. During the photocatalytic evaluation, the photocatalytic system employing 0.5% CuTCPP/$P25_m$ (CuTCPP account for 0.5% in the total amount) engendered approximately 46 times higher methane than generated by $P25_m$ alone. This impressive amelioration can be attributed to a strengthened capability of CuTCPP/$P25_m$ in light absorption and enhanced separation efficiency of photo-induce electrons and holes.

1. Introduction

Nowadays, undue CO_2 discharge has brought about egregiously environment problem like global warming, frequent natural disasters and inclement weather conditions. Seeking for an efficacious way to address these dilemmas becomes one of the most urgent needs for human being to rebuild a harmonious environment. Employing CO_2 as reactant in photocatalytic reduction of it is a promising strategy for clean, cost-effective, and environmentally friendly conversion of CO_2 into hydrocarbon fuels (CH_4, CO, CH_3OH, etc.) assisted by solar energy [1]. Thereby, Many commonly-seen semiconductor materials such as TiO_2 [2], ZnO [3], g-C_3N_4 [4], CdS [5,6] and bismuth-based materials [7–11] have been employed as photocatalysts in this promising conversion of CO_2.

Amid those efficacious materials in photocatalysis, commercial P25 (TiO_2) draws marvelous attention due to its nontoxicity, chemical stability and high photocatalytic activation. However, P25 can only be excited by UV light due to the wide band gap (3.2 eV) of it and with inefficient utility of solar light, thus greatly restricting its application in photocatalysis [12]. In order to overcome such problem, various modification methods like photosensitization [13], semiconductor composite [14], metal and noble metal loading [15,16], have been extensively explored, giving significantly improved results. Among them, method of photosensitization proved to be an effective way to extend the photo-response of semiconductor towards visible region, He et al. prepared dye-sensitized MOF composite and found a evidently increased hydrogen evolution in photocatalytic water splitting under visible-light illumination [17]. Zhang' group investigated highly asymmetric phthalocyanine that played a role of sensitizer for graphitic carbon nitride, which give an enhanced photocatalytic ability in water splitting process assisted by near-IR light of solar radiation [18].

In addition, porphyrin molecules containing carboxylic groups such as tetra(4-carboxylphenyl)porphyrin (TCPP) can be strongly combined onto the metal oxides when there are more hydroxyl on their surfaces, presenting impressively improved photocatalytic activities during their further applications [19]. The sensitized metal oxides are capable of capturing photons more easily and subsequently facilitating the excited state generation in photocatalyses like alcohol oxidation [20], degradation of organic pollutant [21] and hydrogen evolution [22]. Besides, previous research suggested that CO_2 chemical adsorption and

---

activation over Cu^{2+} played an important role in improving the CO_2 conversion efficiency [23]. Meanwhile, after coordinating with metal ion to form metallic complex, the sensitizing effect toward semiconductors would be dramatically modified in comparison with using only porphyrin organic. The carboxyl and phenyl groups in metalloporphyrin are electron withdrawer, and resultantly improve the separation efficiency of photo-excited electrons and holes.

In this study, hydrothermally treated P25 was sensitized by the aforementioned metal complex CuTCPP to synthesize CuTCPP/P25$_m$ composite. Through refluxing with CuTCPP in ethanol together, this sensitizer was successfully combined to P25$_m$ with CuTCPP/P25$_m$ obtained. The as-prepared material exhibits a broadened light absorption range and enhanced charge separation efficiency. Its further application to reduction of CO_2 demonstrates a greatly ameliorated photocatalytic activity. Based on the photocurrent measurements, a possible mechanism of these improved performances was systematically proposed.

2. Experimental

2.1. Materials

TiO$_2$ (P25) purchased from the commercial. Pyrrole (Adamas Reagent Co., Ltd, 99.0%), 4-formylbenzoic acid (Adamas Reagent Co., Ltd, 99.0%) and propionic acid (Adamas Reagent Co., Ltd, 99.0%), were purchased from Damas-beta. CuCl$_2$·2H$_2$O (Sinopharm Chemical Reagent Co., Ltd, 99.0%). All reagents are analytical grade, and without further purification in the process of experiment except pyrrole, which was distilled under reduced pressure before each used. Absolute dimethyl formamide (C$_3$H$_7$NO, DMF, 99.9%), ethanol and methanol were all purchased from Sinopharm Chemical Reagent Co., Ltd, which used as reaction solvent and washing solvent.

2.2. TiO$_2$ (P25) treatment

Commercial P25 through hydrothermal treatment and the specific method according to the literature is as follows [24]: 1.0 g of P25 powder was added to 25 ml distilled water, and continually stirred vigorously for 0.5 h. Afterwards, the mixture was transferred into 50 ml Teflon-lined steel autoclave which was seal to room temperature and kept at 150 °C for 10 h and then cooled. The precipitate was centrifugally separated and washed with distilled water for more than five times. The product dried at 80 °C to obtain the hydrothermally treated P25 powders.

2.3. Preparation of TCPP

The preparation of porphyrin was synthesised according to the previously reported methods in the literature [25]. To the solution of 4-formylbenzoic acid (6.08 g, 40.5 mmol), pyrrole (2.8 g, 40.5 mmol), 150 mL propionic acid were keeping refluxed for 2 h. The reaction black solution was subsequently cooled down to room temperature and added into 200 mL of methanol and stirred for 0.5 h ice bath. The resulting precipitate was centrifugally separated and washed with methanol and warm distilled water several times until the filtrate was clear. The obtained purple powders were finally dried in an oven at 80 °C for 12 h (Yield: 16%).

The spectral data of TCPP were as follows ^{1}**H-NMR** (600 MHz, DMSO-d$_6$, ppm): δ 8.79 (s, 8H); 8.33 (d, 8H); 8.26 (d, 8H) (Fig. S1); UV-Vis (alcohol): λ$_{max}$/nm 415 (S band) and 512, 547, 590, 645 (Q bands); FT-IR (KBr): ν $_{max}$/cm^{-1} 3315, 965 (N-H).

2.4. Preparation of CuTCPP

Copper(II) complex of meso-tetra(4-carboxyphenyl) porphyrin was synthesized according to a reported procedure [26]. The mixture of TCPP (0.261 g, 0.33 mmol) and CuCl$_2$·2H$_2$O (0.31 g, 1.82 mmol) were

dissolved in 15 ml DMF and further refluxed for 5 h. The achieved red solution was cooled to room temperature to give precipitated solid, which was centrifuged and washed with water more than 5 times. Drying the washed compound in vacuum at 60 °C gave a red solid (Fig. S2).

2.5. Preparation CuTCPP/P25$_m$

Typically, 0.60 g P25$_m$ was added in 30 mL ethanol with to form a homogeneous solution. Meanwhile, an appropriate amount of as-prepared CuTCPP sample was dispersed in the solution. The obtained solution was refluxed 5 h at 90 °C, the cooled mixture was filtered and the samples were then washed with ethanol to remove unbound CuTCPP, then centrifugally separated and dried at 80 °C overnight to obtain targeted product. This process yielded different mass ratios of CuTCPP to CuTCPP/P25$_m$, which were labeled as 0.1%, 0.3%, 0.5%, 1%, 1.5%, 2% CuTCPP/P25$_m$. The synthesis procedure of CuTCPP/P25 was similar with above shown.

2.6. Characterizations

Power X-ray diffraction (XRD) data pattern were recorded on a Rigaku D/Max-2400/PC equipped with Cu Kα radiation (40 kV, 20 mA) with scattering angle ranging from 5° to 80°. Fourier transform infrared (FT-IR) spectroscopy with KBr tablet was conducted on a Nicolet NEXUS 670 spectrometer in the wavenumber range of 4000-400 cm^{-1}. Using Ba$_2$SO$_4$ as the internal reflectance standard, the optical properties were measured by double-beam UV-vis spectrophotometer (PuXin TU-1901) equipped with an integrating sphere attachment. The photoluminescence (PL) spectrum detection of samples were conducted on a PELS-55 luminescence/fluorescence spectrophotometer. Surface morphology of all composites was observed by JSM-6701E field emission scanning electron microscope (FE-SEM, Ultra Plus, Carl Zeiss, Germany) with the accelerating voltage of 20 kV after gold sputtering, as well as transmission electron microscopy (TEM, a JEOL model JEM2010 EX microscope at an accelerating voltage of 200 kV). Specific surface areas and pore size distributions were calculated by using N$_2$ adsorption-desorption isotherms and Brunauer-Emmett-Teller (BET) method (the samples were degassed at 80 °C prior to BET measurements).

2.7. Photocatalytic reaction procedures

The photocatalytic reduction of CO_2 with H$_2$O was carried out in a stainless-steel reactor (volume, ~50 mL) with a quartz window on the top of the reactor. Generally, during each run, 2 ml distilled H$_2$O was first filled into a stainless-steel reactor. A glass container (40 × 25 mm) loaded with 0.1 g catalyst was afterwards encased in the reactor. The reaction setup was purged by pure CO_2 and vacuum-treated several times to ensure all the impurities and trapped air were completely removed. Then the photocatalytic reactions were processed by irradiation assisted by light source (300 W Xe lamp, Beijing Au light Co., Ltd. CEL-HXF300/CEL-HXUV300). The reaction temperature was kept at ca. 20℃ by a jacket around the reactor equipped with a circulating cold water bath. The photocatalytic reaction was typically performed for 1 h before the given products (CO/CH$_4$) was collected with extraction syringes and measured by GC-2080 gas chromatography. Flame ionization detector (FID) was adopted to respectively quantify the amounts of CO and CH$_4$ generated from CO_2 reduction.

2.8. Photoelectrochemical performance

Photoelectrochemical performance measurements were carried out on CHI 660D electrochemical workstation (CHI Shanghai) with typical three electrodes cell under the 300 W Xenon lamp as light source illumination. 0.5 M Na$_2$SO$_4$ was employed as electrolyte. The samples P25, TCPP/P25$_m$ and CuTCPP/P25$_m$ were adhered to conductive glasses in a
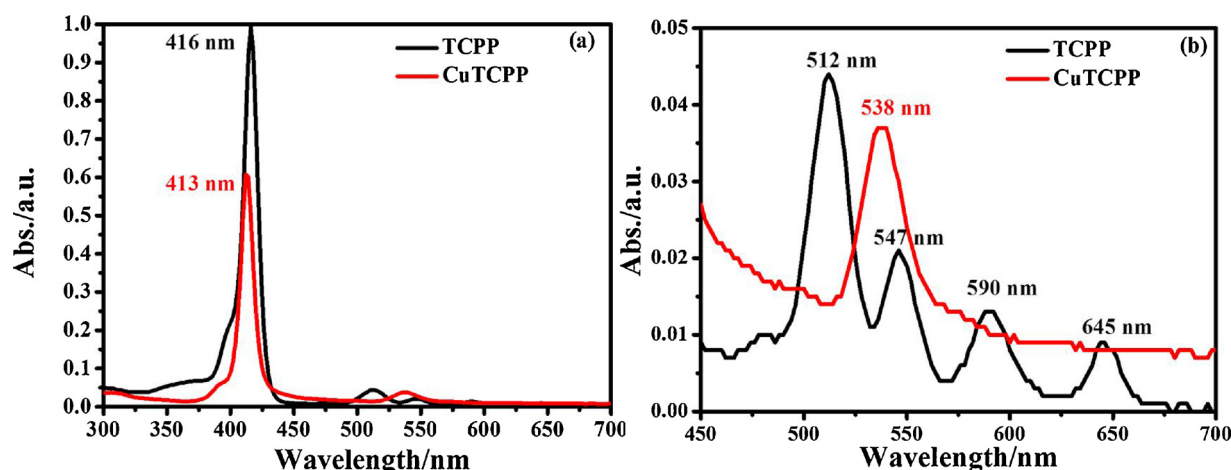
Fig. 1. UV-vis spectra of TCPP and CuTCPP dissolved in ethanol solution (a) UV-vis spectra in the range of 300-700 nm; (b) UV-vis spectra in the range of 450-700 nm.

film solution and then dried under infrared light. Three electrodes were working electrode of photoanodes, Ag/AgCl as reference electrode and wire slice as assistance electrode, respectively. All of the measurements were irradiated from the back side of working electrode with about $1\,cm^{-2}$ areas [27].

3. Results and discussion

3.1. Structure and morphology

Fig.1 shows UV-vis absorption bands of TCPP and CuTCPP in alcohol solutions. Owing to the molar extinction coefficient of the Soret band is much larger than those of the Q bands, the Q bands of the compounds are insignificant (Fig. 1a). In this regard, scanning wavelength range was conducted to give intensified peaks, as shown in Fig. 1b. Soret band of TCPP situates at 416 nm, which results from the transition of a_{1u} (π) to e^*_g (π) (S band). The peaks with less intensity at 512 nm, 547 nm, 590 nm and 645 nm are Q band and corresponding to the a_{2u} (π)-e^*_g (π) transition [28]. In comparison with the spectra of TCPP, the number of Q bands of CuTCPP decrease. Two new peaks arise at 413 nm and 538 nm, indicating the formation of metalloporphyrin [20,29]. It is presumably due to the π-π^* transition that result in electron absorption energy of the conjugated π-orbitals around the porphyrin ring. In porphyrin ligands, two of the four N atoms of the porphyrin ring are connected to uncoordinated N atoms are connected with two hydrogen atoms, thereby reducing the molecular symmetry and reducing the degenerate orbital energy levels with four Q-band absorption peaks presented. In contrast, when four N atoms are is coordinated with central Cu metal ions, so that the molecular structure of the porphyrin complex is symmetric and the energy level is close with the disappearance of Q-band [17].

The surface morphology of pristine P25 and CuTCPP/P25$_m$ were identified in the SEM images Fig. 2a-b. However, more aggregation of P25$_m$ crystallites was clearly observed after hydrothermal treatment for 10 h. The formation of more aggregates may be related to the change of surface properties of the P25 crystallites. According to SEM and TEM images, P25$_m$ formed uniform spherical nanoparticles and the morphology rarely has changed after CuTCPP being loaded. The TEM images of P25 powders before and after hydrothermal treatment are shown in Fig. 2c-d and Fig. S4, indicating that no significant change has been found due to the treatment. The HR-TEM image of the CuTCPP/P25$_m$ composite is exhibited in Fig. 2e. The lattice fringes with spacing of 0.3247 nm and 0.3472 nm are able to clearly observed, which can be indexed to anatase (110) crystal plane and rutile (101) crystal plane [24]. Fig. 2f is EDS analysis of CuTCPP/P25$_m$, confirming that the

nanocomposite is composed of Cu, Ti, O, N and C elements. The elemental mappings of CuTCPP/P25$_m$ detected by energy dispersive X-ray spectroscopy (EDS) demonstrated that all the elements are evenly distributed (Fig. S3).

XRD analysis was conducted to study the crystallinity of as-prepared nanomaterial. All the samples were composed of both rutile and anatase phases as shown in Fig. 3a. The similarity of peaks between P25 and CuTCPP/P25 suggests that the modified composite has maintained the crystallinity of P25. Fig. 3b shows the nitrogen adsorption-desorption isotherms and pore size distributions of the P25 and P25$_m$. It can be seen that both samples show a type H3 hysteresis according to BDDT classification, giving the presence of mesopores (2-50 nm). The observed hysteresis approaches to $P/P_0 = 1$, suggesting the emergence of large pores (> 50 nm). The pore size distributions (inset) demonstrate a wide range from 20 to 100 nm. In fact, P25 powder, produced through hydrolysis of $TiCl_4$ in a hydrogen flame, does not contain pores in each TiO_2 crystallites. Therefore, the formation of the pore structures in the samples could be attributed to the aggregations of TiO_2 crystallites [30]. In other words, the average pore diameter will coincide with the change of TiO_2 crystallite size. An obvious increment of the pore volume of larger pores (10-100 nm) can be observed after hydrothermal treatment, owning to the formation of aggregation of larger P25 crystallites. Textural parameters derived from the nitrogen adsorption-desorption isotherm data are summarized in Table S1. Compared with the P25 precursor, the S_{BET} and the average pore size increased as well [31]. Fig. S5 indicates the spectrum of CO_2 adsorption, which suggests a enhanced capacity of CuTCPP/P25$_m$ for capturing CO_2 rather than that of the reported P25 (TiO_2) [32].

Fig. 4a shows the FT-IR spectra of the TCPP and CuTCPP. The N-H stretching vibration peak is located at near 3315 cm^{-1} in the infrared spectrum of porphyrin compound, while the N-H bending vibration peak with a weak absorption appears at 965 cm^{-1}. Compared to porphyrin ligand, the emergence of peaks near 3315 cm^{-1} and 965 cm^{-1} indicates that the metalloporphyrin complex has been formed [33]. When the metal ions were coordinated with the porphyrin ring, a deformation of vibration would arise and thus generate Cu-N stretching vibration characteristic peak near 1000 cm^{-1}.

The FT-IR spectra of pure P25 and CuTCPP/P25 composites are shown in Fig. 4b. The corresponding signals of CuTCPP/P25 are in accordance with those of CuTCPP, demonstrating that Cu complex has been successfully combined to P25. The peak at 3420 cm^{-1} can be subjected to the stretching vibrations of surface hydroxyl groups P25. Broad peaks ranging from 800 to 500 cm^{-1} are assigned to the Ti-O-Ti stretching vibrations, which can be also seen in the spectra of P25, CuTCPP/P25 and pristine TiO_2. With respect to patterns of Fig. 4b, a
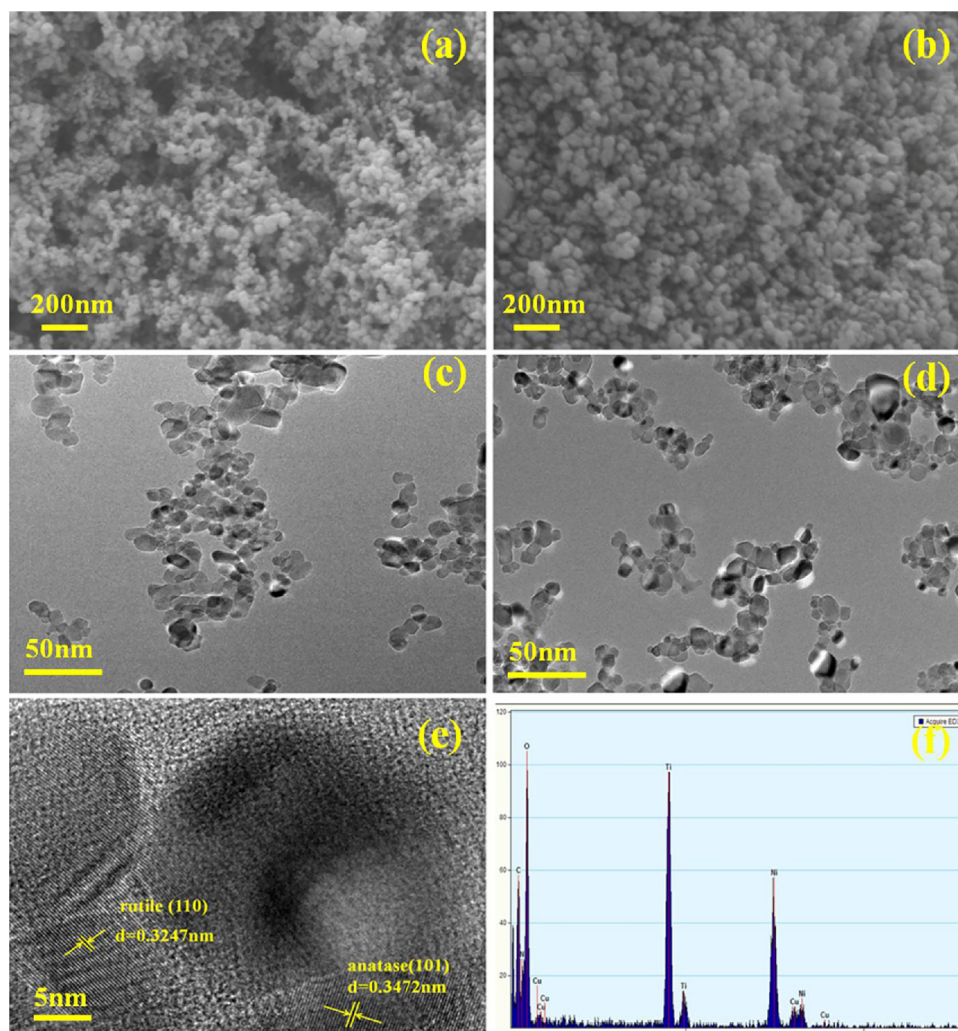
Fig. 2. SEM images of P25 (a) and CuTCPP/P25$_m$ (b), TEM images of P25 (c) and P25$_m$ (d), HR-TEM image of CuTCPP/P25$_m$ sample (e), EDS spectrum of the CuTCPP/P25$_m$ (f).

weak IR peak around 1720-1620 cm^{-1} of CuTCPP/P25 was precisely situated and can be attributed to the -COOH in CuTCPP and Ti-O bond in P25 [23]. In addition, besides the typical peaks of TiO$_2$, distinctive peaks of CuTCPP can also be observed at ca.1000 cm^{-1} in the FT-IR

spectra of CuTCPP/P25 (Fig. 4c) [26].

The composition and chemical state of the 0.5% CuTCPP/P25$_m$ composite were investigated by XPS. The survey spectrum (Fig. 5a) indicates that the sample is composed of C, N, Ti, O and Cu, agreeing
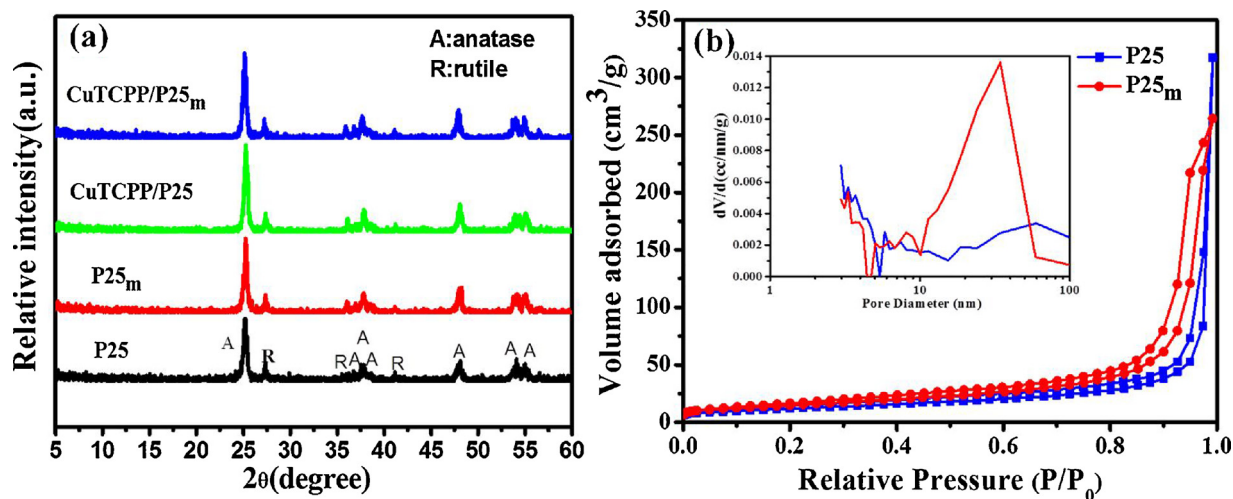

Fig. 3. (a) XRD patterns of the P25, P25$_m$, CuTCPP/P25 and CuTCPP/25$_m$, (b) The nitrogen adsorption-desorption isotherms and corresponding pore size distributions (inset) of the P25/P25$_m$.
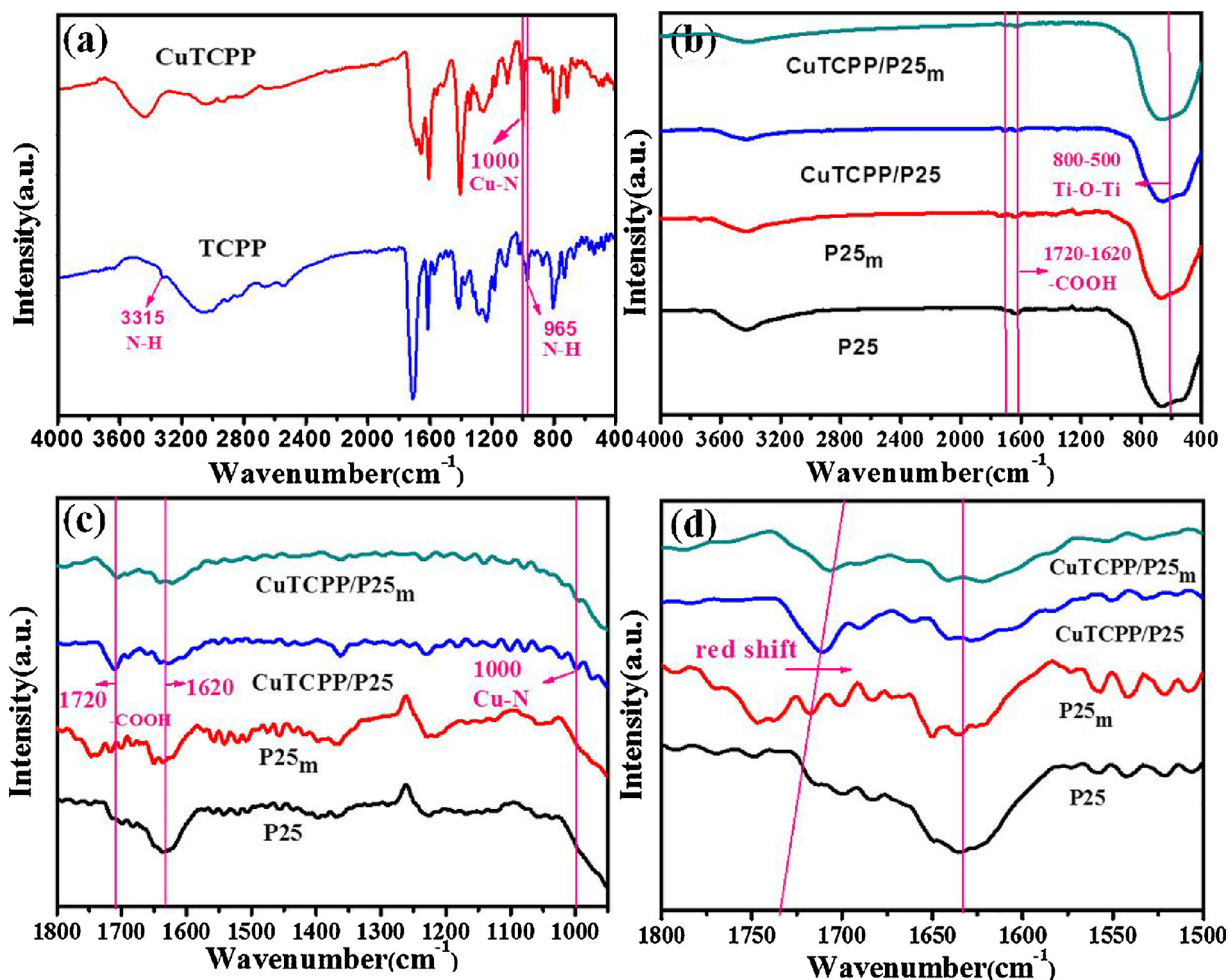
Fig. 4. (a) FT-IR spectra the synthesis TCPP and CuTCPP, (b-d) FTIR spectra of P25, P25$_m$, CuTCPP/P25 and CuTCPP/P25$_m$ in different ranges of wavenumbers.
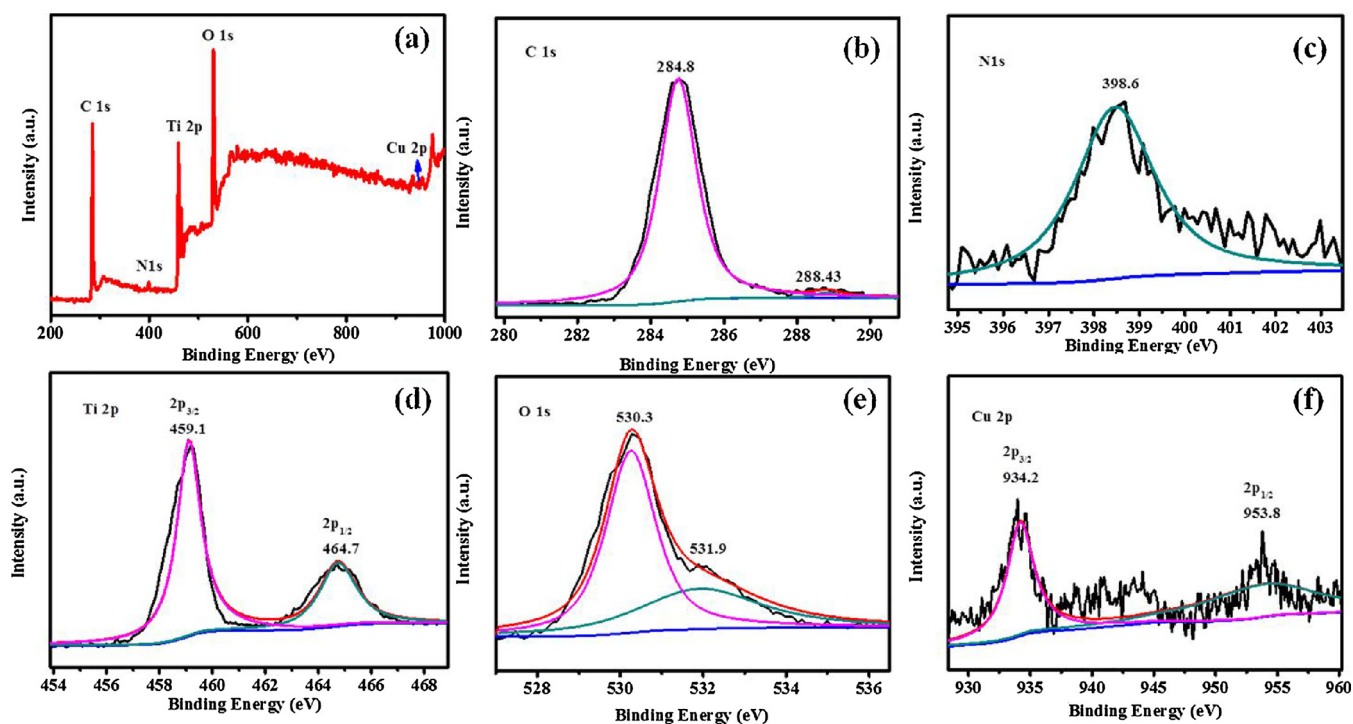

Fig. 5. XPS spectra of 0.5% CuTCPP/P25$_m$: (a) survey, (b) C 1 s, (c) N 1 s, (d) Ti 2p, (e)O 1 s, (f) Cu 2p.

well with the EDX and mapping results. Fig. 5b shows the binding energies of C 1 s peaks are at 284.8 and 288.43 eV, respectively. The N 1 s (Fig. 5c) is located at 398.6 eV. In Fig. 5d, high-resolution Ti 2p spectrum with two peaks can be ascribable to both Ti $2p_{3/2}$ at 459.1 eV and Ti $2p_{1/2}$ at 464.7 eV. The O 1 s XPS spectra (Fig. 5e) can be attributed to lattice oxygen (530.3 eV) in P25 and -OH species (531.9 eV). The signals of Cu 2p region (Fig. 5f) can be deconvoluted into two peaks for Cu $2p_{3/2}$ and $2p_{1/2}$, which are located at around 934. 2 eV and 953.8 eV, respectively [34].

3.2. Anchoring group CuTCPP/P25$_m$ composite

After hydrothermal treatment towards commercial P25, surface hydroxyl has been significantly increased. In this way, more CuTCPP can be combined to P25$_m$ to form relatively stable composites, as indicated in Fig. S6 [35]. The possible binding modes between CuTCPP and P25$_m$ surface are exhibited in Fig. S7. Carboxylic acid in the meso-positions of porphyrin ring is an anchoring group that has been extensively studied. There are two main classes of linking modes between porphyrin derivative with carboxylic group and TiO$_2$ that have been employed quite often, unidentate coordination, anchoring mode [36]. Unidentate coordination of the carboxylate group will remove the equivalence of the two oxygen atoms, resulting in an ester type of bond formation between the carboxylic acid group and the P25 surface, while anchoring mode is either chelation or bridging bidentate as shown in Fig. S9 [37]. According to FT-IR spectra, if the difference between the carboxylate group asymmetric and symmetric stretching mode bands in the adsorbed state is less than that in the free solid state, the anchoring mode will dominate the binding method, and if the opposite applies, the anchoring mode is unidentate [38]. Also, the difference shown by FT-IR spectra of CuTCPP/P25$_m$ between these bands in the deprotonated porphyrins (≈ 244 cm^{-1}) and the adsorbed porphyrins (≈ 207 cm^{-1}), along with other evidence that provide the presumption in which the chelation mode is unstable. Thus, the carboxylate groups are connected to the surface of P25$_m$ via a bridging bidentate mode [20].

Due to the published literature [39], the formation of hydrogen bonds (Fig. S8), will average the electron cloud density, leading to a diminishment in the stretching vibration frequency. As suggested in the FT-IR spectra of CuTCPP/P25$_m$ (Fig. 4d), the absorption peak of the proton donor largely shifts from 1725 cm^{-1} of P25$_m$ to a lower wave number range 1750-1700 cm^{-1} of CuTCPP/P25$_m$, probably suggesting that hydrogen bonds were formed between hydroxyl groups on the surface of P25$_m$ and carbonyl groups of CuTCPP, thus strongly augmenting their intermolecular interactions [29].

3.3. PL, DRS and PEC characterizations

To measure separation and recombination performances of the photo-excited electron-hole pairs of the as prepared compounds, photoluminescence spectra (PL) were finely conducted (Fig. 6a) [40]. A strong peak is observed in the PL spectrum at 450 nm of pure P25$_m$, while no such signal can be seen in the spectrum of CuTCPP. After the combination, CuTCPP/P25$_m$ composite presents an obvious peak at 450 nm, but weaker than that of P25$_m$, showing a fluorescence quenching impact exerted by CuTCPP on P25$_m$, which are thus presumably ascribable to a greatly suppressed recombination of the photo-induced charge carriers. Fig. 6b shows the UV-vis diffuse reflectance spectroscopy (DRS) of P25 and P25$_m$. A slight red shift from spectrum of P25 to that of P25$_m$ demonstrates a decreased band gap energies of the hydrothermally treated P25 powders compared to pristine P25, and that hydrothermal treatment can obviously affect the light absorption characteristics of P25. In other words, hydroxylation of TiO$_2$ might incur a change the surface microstructure, composition and phase structure of the powder [41,42]. CuTCPP/P25$_m$ sample possesses strong absorption in visible region (400-700 nm) with a strongest intensity at the peak of 413 nm and less intense one at the peak of 543 nm, both of

which are ascribed to the combined porphyrin. The CuTCPP/P25$_m$ composite shows hybrid absorption features of both CuTCPP and P25$_m$, which allows a more efficient utilization of the solar spectrum to create photo-generated electrons and holes. The results of time-resolved PL spectroscopy were shown in Fig. S10 and Table S2. The average lifetime of the samples increased from 0.954 ns for P25$_m$ to 1.922 ns for 0.5% CuTCPP/P25$_m$. The prolonged lifetime of charge carriers could be explained by both the expedition of the migration of charge carriers and further enhancement of the charge carriers' separation [43].

In order to explore the influence of CuTCPP on the charge separation efficiency of P25, photocurrents of pure P25$_m$ and 0.5% CuTCPP/P25$_m$ composite dripped onto FTO electrodes are measured, as shown in Fig. 7a. The photocurrent boosted rapidly when the light was turned on and finally remained a relative constant value. In contrast, when the light was turned off, photocurrent instantaneously declined to zero [44]. Obviously, the photocurrent generated by the CuTCPP/P25$_m$ composite is much higher than that of P25$_m$, indicating that the charge separation efficiency of P25$_m$ can be effectively promoted. The Linear current-voltage (LSV) curves of P25$_m$ and CuTCPP/P25$_m$ photoanodes are recorded in Fig. S11. The photocurrent density of CuTCPP/P25$_m$ increased when the light was on. Electrochemical impedance spectroscopy (EIS) of P25$_m$ and CuTCPP/P25$_m$ was operated to explore transfer properties of charge carries and enhanced photoelectrochemical (PEC) performance, as shown in Fig. 7b-c. The Nyquist plots shows a significant decrement of electrochemical impedance value from electrode P25$_m$ to CuTCPP/P25$_m$, suggesting that the combined sensitizer is able to enlarge the visible light absorption capacity of P25$_m$ and benefit the transfer and separation of photo-induced carriers. The semicircle of the CuTCPP/P25$_m$ is smaller than P25 electrode in both dark and illuminating condition, demonstrating that CuTCPP/P25$_m$ embraces a higher efficiency of electrons and holes transport in the interface between semiconductor and electrolyte [41,45].

3.4. Photocatalytic CO$_2$ reduction performance

In order to explore the impact of the combined CuTCPP on the photocatalytic activities of P25 and P25$_m$, a list of the photocatalytic CO$_2$ reduction have been carried out under 300 W Xe lamp, as well as under visible light (Fig. 8). It can be seen the sensitization can result in an enhanced reduction of CO$_2$ mainly into CH$_4$ rather than that dominated by either P25 or P25$_m$. To illustrate, pure P25 produced 0.27 μmol/g/h CH$_4$ and 0.75 μmol/g/h CO, while P25$_m$ produced 0.42 μmol/g/h CH$_4$ and 1.7 μmol/g/h CO (Fig. 8a-b). The increment achievements may be relevant to the increased surface hydroxyl groups that are able to absorb more amount of the mixture of CO$_2$ and H$_2$O via hydrogen bond after hydrothermal treatment. When untreated P25 was sensitized by 0.5% CuTCPP and irradiated with 300 W Xe lamp, 15.5 μmol/g/h CH$_4$ and 2.3 μmol/g/h CO were generated (Fig. 8a). Expectedly, as the hydrothermally treated P25 was sensitized by 0.5% CuTCPP, more yields were achieved from the photocatalytic reduction, 19.39 μmol/g/h for CH$_4$ and 2.68 μmol/g/h for CO (Fig. 8b). It is found that the total CO and CH$_4$ evolution increased with increment in the amount of combined CuTCPP. When the ratio of CuTCPP in the composite was 0.5%, a maximum reduction yields would be obtained. However, as the amount of CuTCPP continued to increase, the product amounts of both CO and CH$_4$ would descend (Fig. 8a-b). It can be explained that the initial raise in the combined CuTCPP is able to more effectively sensitize P25$_m$ and subsequently enhance the photocatalytic activity. Nonetheless, the reduction reaction mainly takes place on the surface of P25$_m$ (Fig. S12) [28]. Excess combination of CuTCPP on the surface would greatly reduce the reactive sites and thus bring about abatement in the reaction product. To determine the effect of sensitization on photocatalysis under visible light, the photocatalysis reduction of CO$_2$ were carried out at the wavelength above 400 nm. Generally, the amount of both products of the reactions was significant decreased. Few yields of either CH$_4$ or CO were detected in P25$_m$
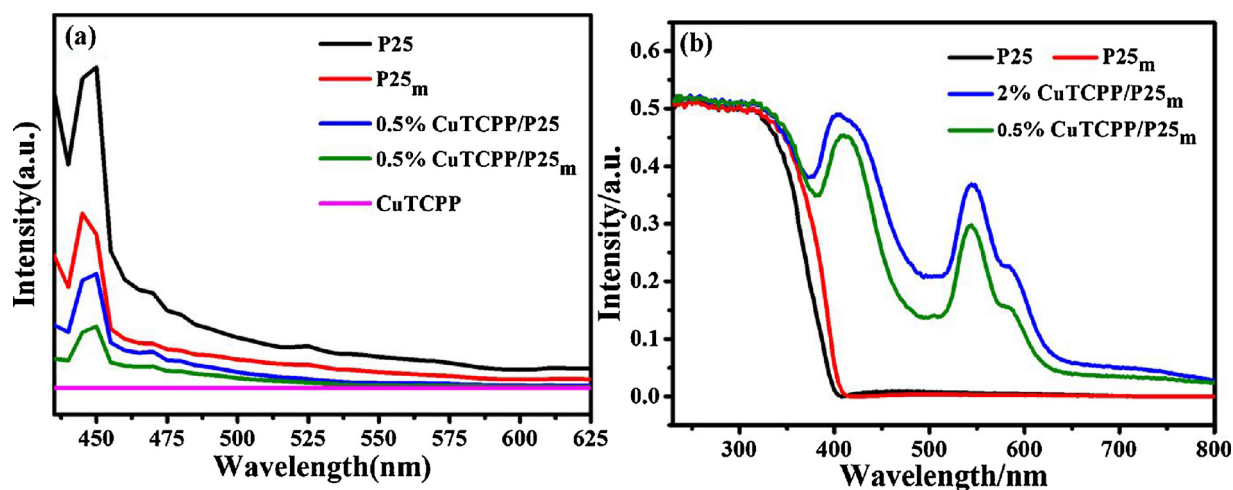
Fig. 6. (a) PL spectra of pure P25 and composite (excitation wavelength: 415 nm), (b) UV-vis diffuse reflectance spectra of pure P25 and composite.
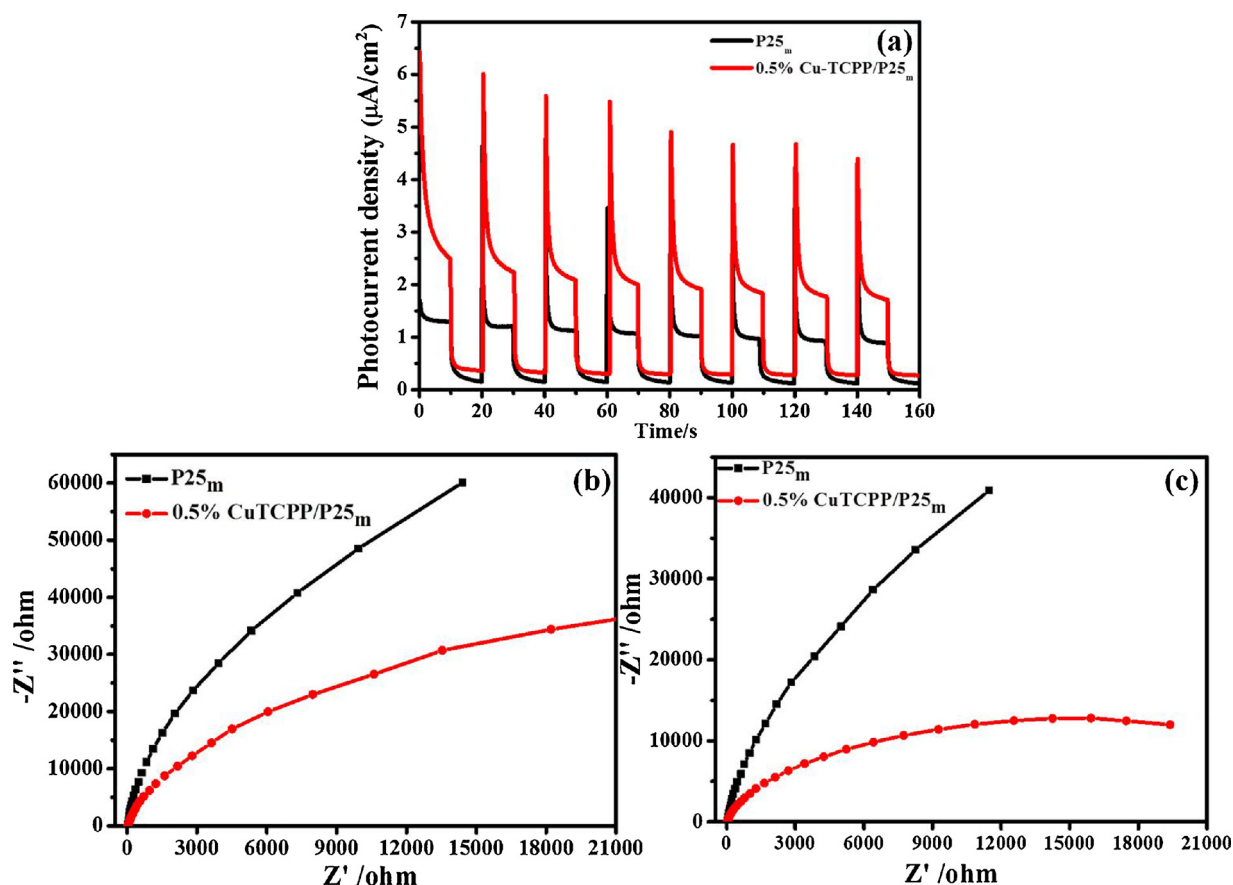

Fig. 7. (a) Photocurrent response of the P25 and 0.5% CuTCPP/P25; Nyquist plots of EIS measurements on the P25 and CuTCPP/P25$_m$ electrodes: (b) in the dark and (c) light irradiation (0.5 M Na$_2$SO$_4$).

conducting photocatalytic reduction, mainly owning to the primary light response locating in the range of the wavelength that is less than 380 nm [46]. Nevertheless, the sensitizing impact is still observable and apparently indicated by the evolution of 2.24 μmol/g/h CH$_4$ and 0.85 μmol/g/h CO in the 0.5% photocatalytic reduction of CO$_2$ catalyzed with CuTCPP/P25$_m$ (Fig. 8c).

In order to indicate the catalytic activity of TCPP or CuTCPP alone, the light-irradiation activity of TCPP and CuTCPP were employed as photocatalysts, respectively (Fig. 8d). The results indicate that few products has been produced. In addition, for explicitly demonstrating the photocatalyst's stability, the reaction system loading with 0.5%

CuTCPP/P25$_m$ was operated under the atmosphere of either Ar or CO$_2$ at the time intervals of 5, 15, 30 and 60 min, respectively (Fig. S13). While the reactor was filled with Ar gas, a small amount of CO can be detected in an increasing trend at these four intervals due to the slight decomposition of organics initiated that might be initiated by the UV-light irradiation [47] or the photo-generated carriers [48]. However, in comparison to the highly increasing generation of CH$_4$ under the CO$_2$ atmosphere, no signal of CH$_4$ can be found in the dispersion of Ar at both the intervals of 5 and 15 min. Only at the intervals of 30 min and 60 min, small amounts of almost equivalent productions of CH$_4$ were given. When the catalytic process was prolonged up to 12 h in the
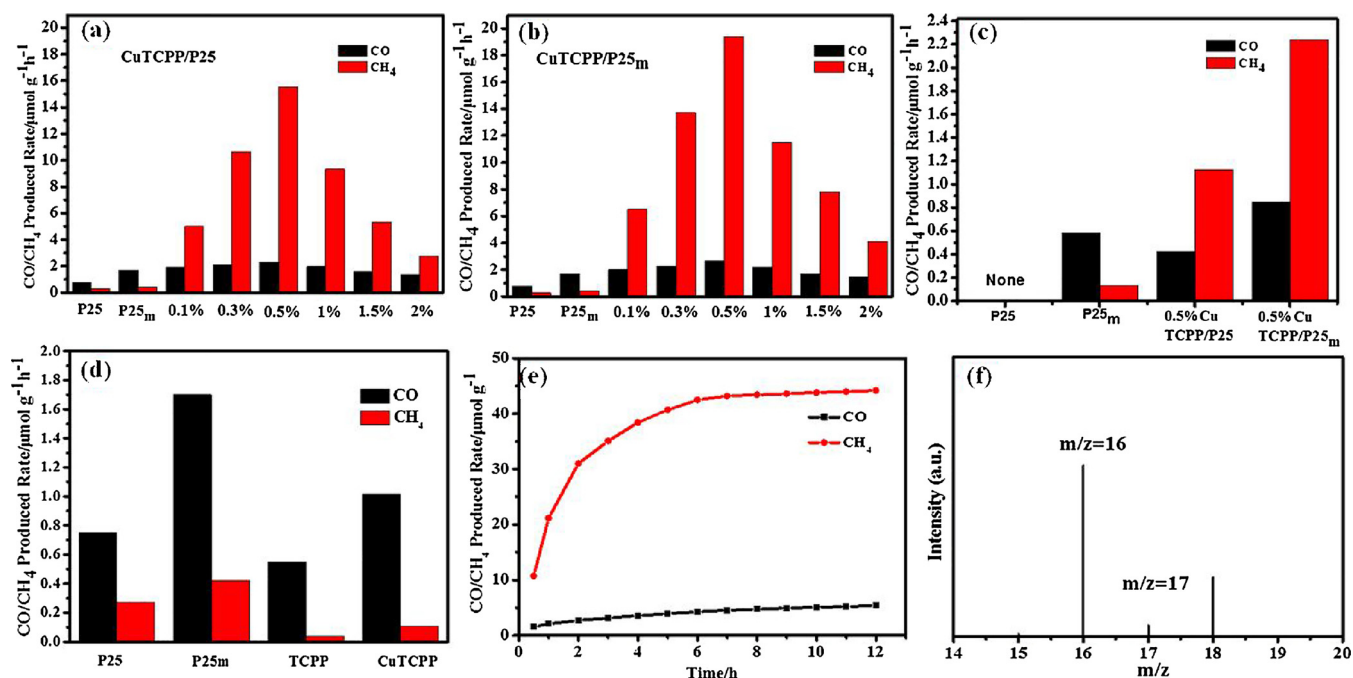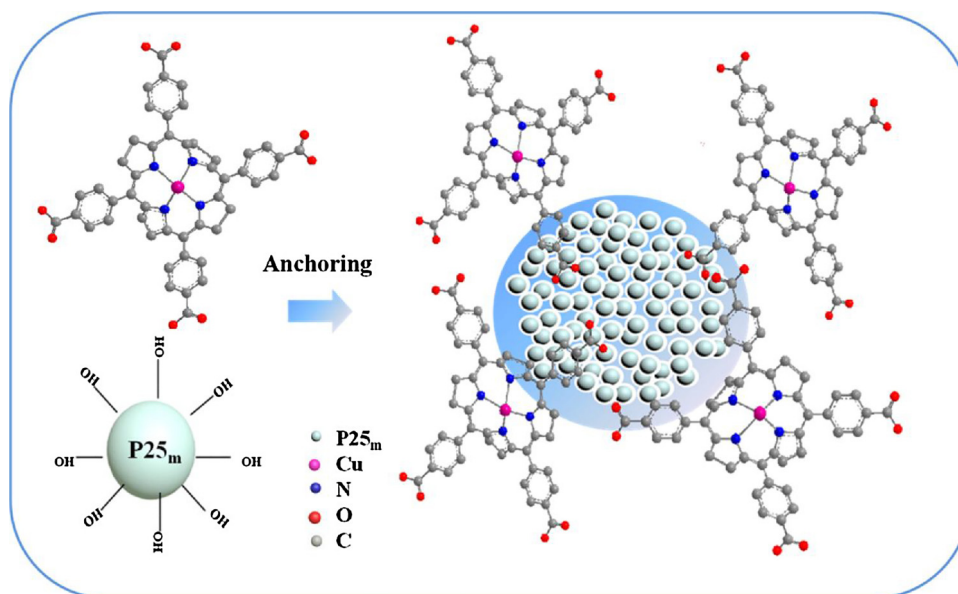
Fig. 8. Dependence of (a) and (b) total CO/CH$_4$ evolution amount within 1 h with the amount of CuTCPP/P25 or P25$_m$ (0.1%, 0.3%, 0.5%, 1%, 1.5% and 2%, respectively) with 300 W Xe lamp, (c) 0.5% CuTCPP/P25 or P25$_m$ under visible-light illumination (λ > 400 nm), (d) the catalytic activity of TCPP and CuTCPP, (e) total CO/CH$_4$ evolution amount of 0.5% CuTCPP/P25$_m$ with 300 W Xe lamp within 12 h, (f)the GC-MS patterns of the produced CH$_4$ over 0.5% CuTCPP/P25$_m$ using $^{13}CO_2$ after 2 hours.
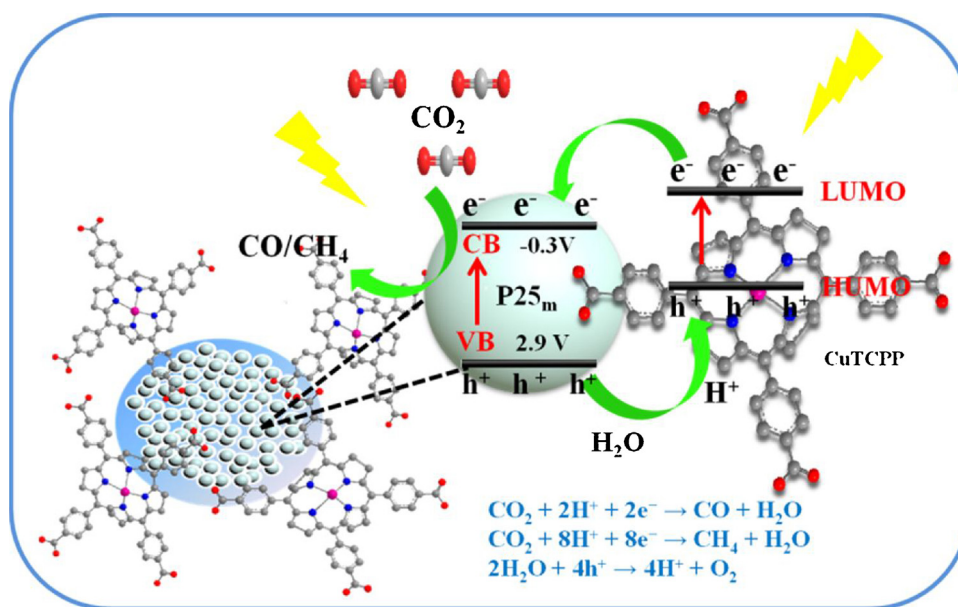

Scheme 1. Schematic illustration of the preparation of the CuTCPP/P25$_m$ photocatalyst.

presence of CO_2 (Fig. 8e), an obvious increment of CH$_4$ evolution can be seen in the first six hours. Nevertheless, for the remained six hours, the producing speeding was slowing down significantly. Therefore, although the combined CuTCPP might decompose during the photo-catalytic process, the major carbon source for producing CH$_4$ should still be the extraneous CO_2 filled in the reactor, especially within the first couple hours of the reaction when the decomposition of CuTCPP is relatively negligible. Besides, isotope tracer experiment involving photo-reduction of $^{13}CO_2$ (Fig. 8f) present a peak that can be assigned to $^{13}CH_4$ (m/z = 16 and 17), also confirm our consideration above [34]. With respect to the structure composition of the composites, the quite proximity of the spectra of PEC, FT-IR and XRD between pristine

0.5% CuTCPP/P25$_m$ and used one demonstrates that CuTCPP still presented after the 1-hour photocatalytic process (Fig. S14-S15) (Scheme 1).

3.5. Electron transfer and photocatalytic mechanism

Based on the above results, a possible mechanism for CO_2 photo reduction over CuTCPP/P25$_m$ heterogeneous catalysts under 300 W Xe lamp, as well as that reasoned from the catalysis under visible light were both proposed in Scheme 2. In the beginning, P25 were hydro-thermally treated, resulting in an enlarged specific surface area and increased hydroxyl on the surface of P25$_m$, both of which contributed

Scheme 2. The possible mechanism of reduction of CO_2 into CH_4/CO photocatalyzed by $CuTCPP/P25_m$.

much to a raised adsorption of CO_2 [24]. When exposed to 300 W Xe lamp, both CuTCPP and $P25_m$ of the composite can be excited to generate electrons and holes. The LUMO position of CuTCPP is sufficiently negative than conduction band (CB) of $P25_m$, while HUMO position of CuTCPP is lower than valance band (VB) of $P25_m$ [23]. Due to these pertinent band potentials, the photo-generated electrons on the CB of CuTCPP can be injected into that of $P25_m$, which would subsequently be involved in reduction of the adsorbed CO_2. On the other hand, the photo-induced holes on the VB of $P25_m$ can migrate to that of CuTCPP, afterwards reacted with H_2O to give H^+ which plays the role of one reactant in the reaction for generating CH_4 in photocatalysis. As $CuTCPP/P25_m$ was irradiated by visible light, only CuTCPP can be excited, whereas $P25_m$ was not able to be excited owning to its large band gap. The photo-generated electrons on the LUMO of CuTCPP were also capable of transferring to the CB of TiO_2, and thus participating in the photocatalyic reduction of CO_2. Simultaneously, the holes on the HUMO of CuTCPP can react with H_2O to form H^+ as well [49]. Therefore, due to the broadened photo-response range and promoted charge separation rate, the $CuTCPP/P25_m$ composite exhibits enhanced photocatalytic CO_2 reduction activity rather than using $P25_m$ as photocatalyst under 300 W Xe lamp.

4. Conclusions

In summary, the hydrothermally treated P25 nanoparticles were successfully combined to the surface of CuTCPP to obtain the $CuTCPP/P25_m$. As an efficient photosensitizer, CuTCPP can greatly broaden the photo-response ability P25 and improve light energy utilization. The resulted $CuTCPP/P25_m$ composite showed higher yield of CH_4 in photocatalytic reduction of CO_2 either under 300 W Xe lamp or assisted by visible light than that of $P25_m$, probably owing to their strengthened absorption capability to light and improvement on electron-hole separation. The strategy for exploring more active photocatalysts suggested in this work probable applicable to other catalytic systems established to improve photocatalytic efficiency in CO_2 conversion.

Acknowledgements

Appendix A. Supplementary data

Supplementary material related to this article can be found, in the online version, at doi:https://doi.org/10.1016/j.apcatb.2018.08.007.

References

[1] J. Ran, M. Jaroniec, S.Z. Qiao, Adv. Mater. 30 (2018) 1704649.
[2] T. Zhang, J. Low, K. Koh, J. Yu, T. Asefa, ACS Sustain.Chem. Eng. 6 (2018) 531–540.
[3] R. Rahimi, S. Shariatinia, S. Zargari, M.Y. Berijani, A. Ghaffarinejad, Z.S. Shojaie, RSC Adv. 5 (2015) 46624–46631.
[4] G. Zhao, H. Pang, G. Liu, P. Li, H. Liu, H. Zhang, L. Shi, J. Ye, Appl. Catal. B: Environ. 200 (2017) 141–149.
[5] C. Zhu, C. Liu, Y. Zhou, Y. Fu, S. Guo, H. Li, S. Zhao, H. Huang, Y. Liu, Z. Kang, Appl. Catal. B: Environ. 216 (2017) 114–121.
[6] Q. Wang, J. Lian, Q. Ma, S. Zhang, J. He, J. Zhong, J. Li, H. Huang, B. Su, Catal. Today 281 (2017) 662–668.
[7] X. Liu, X. Xiong, S. Ding, Q. Jiang, J. Hu, Catal. Sci. Technol. 7 (2017) 3580–3590.
[8] J. Ding, Z. Dai, F. Qin, H. Zhao, S. Zhao, R. Chen, Appl. Catal. B: Environ. 205 (2017) 281–291.
[9] J. Ding, Z. Dai, F. Tian, B. Zhou, B. Zhao, H. Zhao, Z. Chen, Y. Liu, R. Chen, J. Mater. Chem. A 5 (2017) 23453–23459.
[10] Y. Shi, X. Xiong, S. Ding, X. Liu, Q. Jiang, J. Hu, Appl, Catal. B: Environ. 220 (2018) 570–580.
[11] Y. Zhu, Y. Wang, Q. Ling, Y. Zhu, Appl. Catal. B: Environ. 200 (2017) 222–229.
[12] S. Kumar, M.A. Isaacs, R. Trofimovaite, L. Durndell, C.M.A. Parlett, R.E. Douthwaite, B. Coulson, M.C.R. Cockett, K. Wilson, A.F. Lee, Appl. Catal. B: Environ. 209 (2017) 394–404.
[13] D.I. Won, J.S. Lee, Q. Ba, Y.J. Cho, H.Y. Cheong, S. Choi, C.H. Kim, H.J. Son, C. Pac, S.O. Kang, ACS Catal. 8 (2018) 1018–1030.
[14] X. Ning, J. Li, B. Yang, W. Zhen, Z. Li, B. Tian, G. Lu, Appl. Catal. B: Environ. 212 (2017) 129–139.
[15] A. Razzaq, A. Sinhamahapatra, T.-H. Kang, C.A. Grimes, J.-S. Yu, S.-I. In, Appl. Catal. B: Environ. 215 (2017) 28–35.
[16] X. Cui, Z. Pan, L. Zhang, H. Peng, G. Zheng, Adv. Energy Mater. 7 (2017).
[17] J. He, J. Wang, Y. Chen, J. Zhang, D. Duan, Y. Wang, Z. Yan, Chem. Commun. 50 (2014) 7063–7066.
[18] X. Zhang, L. Yu, C. Zhuang, T. Peng, R. Li, X. Li, ACS Catal. 4 (2013) 162–170.
[19] B. Zhuang, L. Xiangqing, R. Ge, S. Kang, L. Qin, G. Li, Appl. Catal. A Gen. 533 (2017) 81–89.
[20] E. Safaei, S. Mohebbi, J. Mater. Chem. A 4 (2016) 3933–3946.
[21] D. Chen, K. Wang, W. Hong, R. Zong, W. Yao, Y. Zhu, Appl. Catal. B: Environ. 166–167 (2015) 366–373.
[22] M. Zhu, Z. Li, B. Xiao, Y. Lu, Y. Du, P. Yang, X. Wang, ACS Appl. Mater. Interfaces 5 (2013) 1732–1740.
[23] Y. Liu, Y. Yang, Q. Sun, Z. Wang, B. Huang, Y. Dai, X. Qin, X. Zhang, ACS Appl. Mater. Interfaces 5 (2013) 7654–7658.

[24] J. Yu, H. Yu, B. Cheng, M. Zhou, X. Zhao, J. Mater. Chem. A 253 (2006) 112–118.
[25] T. Rhauderwiek, S. Waitschat, S. Wuttke, H. Reinsch, T. Bein, N. Stock, Inorg. Chem. 55 (2016) 5312.
[26] L. Lin, C. Hou, X. Zhang, Y. Wang, Y. Chen, T. He, Appl. Catal. B: Environ. 221 (2018) 312–319.
[27] Q. Wang, J. He, Y. Shi, S. Zhang, T. Niu, H. She, Y. Bi, Chem. Eng. J. 326 (2017) 411–418.
[28] S. Nakashima, R. Negishi, H. Tada, Chem. Commun. 52 (2016) 3665–3668.
[29] R. Ge, X. Li, B. Zhuang, S.-Z. Kang, L. Qin, G. Li, Appl. Catal. B: Environ. 211 (2017) 296–304.
[30] H. Yin, Y. Wada, T. Kitamura, S. Kambe, S. Murasawa, H. Mori, T. Sakata, S. Yanagida, J. Mater. Chem. 11 (2001) 1694–1703.
[31] Y. Liu, G. Zhu, J. Gao, R. Zhu, M. Hojamberdiev, C. Wang, X. Wei, P. Liu, Appl. Catal. B: Environ. 205 (2017) 421–432.
[32] X. Li, Y. Pi, Q. Hou, H. Yu, Z. Li, Y. Li, J. Xiao, Chem. Commun. 54 (2018) 1917–1920.
[33] L. K, L. L, P. T, G. Y, L. R, Z. J, Chem. Commun. 51 (2015) 12443–12446.
[34] F. Xu, J. Zhang, B. Zhu, J. Yu, J. Xu, Appl. Catal. B: Environ. 230 (2018) 194–202.
[35] J. Rochford, D. Chu, A. Hagfeldt, E. Galoppini, J. Am. Chem. Soc. 129 (2007) 4655–4665.
[36] J. Rochford, E. Galoppini, Langmuir 24 (2008) 5366–5374.

[37] E. Galoppini, Chem. Rev. 248 (2004) 1283–1297.
[38] K. Ladomenou, T.N. Kitsopoulos, G.D. Sharma, A.G. Coutsolelos, RSC Adv. 45 (2015) 21379–21404.
[39] K.S. Finnie, J.R. Bartlett, J.L. Woolfrey, Langmuir 14 (1998) 2744–2749.
[40] G. Zhu, W. Que, J. Zhang, J. Alloys Compd. 509 (2011) 9479–9486.
[41] Z. You, Y. Su, Y. Yu, H. Wang, T. Qin, F. Zhang, Q. Shen, H. Yang, Appl. Catal. B: Environ. 213 (2017) 127–135.
[42] J. Yu, J. Xiong, B. Cheng, S. Liu, Appl. Catal. B: Environ. 60 (2005) 211–221.
[43] X. Ning, J. Li, B. Yang, W. Zhen, Z. Li, B. Tian, G. Lu, Appl. Catal. B: Environ. 212 (2017) 0129–0139.
[44] Q. Wang, T. Niu, L. Wang, C. Yan, J. Huang, J. He, H. She, B. Su, Y. Bi, Chem. A Eur. J. 337 (2018) 506–514.
[45] Y. Zhang, S. Zong, C. Cheng, J. Shi, P. Guo, X. Guan, B. Luo, S. Shen, L. Guo, Appl. Catal. B: Environ. 233 (2018) 80–87.
[46] M. Pelaez, N.T. Nolan, S.C. Pillai, M.K. Seery, P. Falaras, A.G. Kontos, P.S.M. Dunlop, J.W.J. Hamilton, J.A. Byrne, K. O'Shea, M.H. Entezari, D.D. Dionysiou, Appl. Catal. B: Environ. 125 (2012) 331–349.
[47] G. Matafonova, V. Batoev, Water Res. 132 (2018) 177–189.
[48] S. Murphy, C. Saurel, A. Morrissey, J. Tobin, M. Oelgemöller, K. Nolan, Appl. Catal. B: Environ. 119–120 (2012) 156–165.
[49] Z. Zhang, H. Liu, J. Xu, H. Zeng, J. Photochem. Photobiol. A 336 (2017) 25–31.